Redox Biology 68 (2023) 102944

Contents lists available at ScienceDirect

Redox Biology

journal homepage: www.elsevier.com/locate/redox

Nogo-B mediates endothelial oxidative stress and inflammation to promote coronary atherosclerosis in pressure-overloaded mouse hearts

Yu Zhang [a,1], Jing-Jing Li [b,1], Rui Xu [c], Xin-Pei Wang [e], Xin-Yi Zhao [a], Yuan Fang [d], Yu-Peng Chen [a], Shan Ma [a], Xiao-Hui Di [c], Wei Wu [a], Gang She [a], Zheng-Da Pang [a], Yi-Dong Wang [b,d], Xing Zhang [e], Wenjun Xie [b], Xiu-Ling Deng [a], Xiao-Jun Du [a], Yi Zhang [a,*]

[a] Department of Physiology and Pathophysiology, School of Basic Medical Sciences, And Key Laboratory of Environment and Genes Related to Diseases, Ministry of Education, Xi'an Jiaotong University Health Science Center, Xi'an, Shaanxi, China
[b] Department of Cardiology, First Affiliated Hospital of Xi'an Jiaotong University, Xi'an, Shaanxi, China
[c] The Key Laboratory of Biomedical Information Engineering of Ministry of Education, School of Life Science and Technology, Xi'an Jiaotong University, Xi'an, Shaanxi, China
[d] The Institute of Cardiovascular Sciences, School of Basic Medical Sciences, Xi'an Jiaotong University, Xi'an, Shaanxi, China
[e] Department of Aerospace Medicine, Fourth Military Medical University, Xi'an, Shaanxi, China

ARTICLE INFO

Keywords:
Nogo-B
Pressure overload
Mitochondria
Reactive oxygen species
Coronary atherosclerosis

ABSTRACT

Aims: Endothelial dysfunction plays a pivotal role in atherosclerosis, but the detailed mechanism remains incomplete understood. Nogo-B is an endoplasmic reticulum (ER)-localized protein mediating ER-mitochondrial morphology. We previously showed endothelial Nogo-B as a key regulator of endothelial function in the setting of hypertension. Here, we aim to further assess the role of Nogo-B in coronary atherosclerosis in ApoE$^{-/-}$ mice with pressure overload.

Methods and results: We generated double knockout (DKO) mouse models of systemically or endothelium-specifically excising Nogo-A/B gene on an ApoE$^{-/-}$ background. After 7 weeks of transverse aortic constriction (TAC) surgery, compared to ApoE$^{-/-}$ mice DKO mice were resistant to the development of coronary atherosclerotic lesions and plaque rapture. Sustained elevation of Nogo-B and adhesion molecules (VCAM-1/ICAM-1), early markers of atherosclerosis, was identified in heart tissues and endothelial cells (ECs) isolated from TAC ApoE$^{-/-}$ mice, changes that were significantly repressed by Nogo-B deficiency. In cultured human umbilical vein endothelial cells (HUVECs) exposure to inflammatory cytokines (TNF-α, IL-1β), Nogo-B was upregulated and activated reactive oxide species (ROS)-p38-p65 signaling axis. Mitofusin 2 (Mfn2) is a key protein tethering ER to mitochondria in ECs, and we showed that Nogo-B expression positively correlated with Mfn2 protein level. And Nogo-B deletion in ECs or in ApoE$^{-/-}$ mice reduced Mfn2 protein content and increased ER-mitochondria distance, reduced ER-mitochondrial Ca^{2+} transport and mitochondrial ROS generation, and prevented VCAM-1/ICAM-1 upregulation and EC dysfunction, eventually restrained atherosclerotic lesions development.

Conclusion: Our study revealed that Nogo-B is a critical modulator in promoting endothelial dysfunction and consequent pathogenesis of coronary atherosclerosis in pressure overloaded hearts of ApoE$^{-/-}$ mice. Nogo-B may hold the promise to be a common therapeutic target in the setting of hypertension.

1. Introduction

Coronary artery disease (CAD) is the leading cause of death and morbidity worldwide [1,2]. Accumulating evidence indicate endothelial dysfunction as a pivotal event contributing to CAD initiation and progression [3–6]. Lining the vascular intima is the endothelium functioning as a barrier separating vessels from circulating blood. Endothelium also acts as an integrator and transducer of humoral and mechanical stimuli to regulate vascular homeostasis [7]. Pro-atherosclerotic factors like hypertension and hypercholesterolemia trigger phenotypic alterations of the endothelium into an inflammatory

* Corresponding author. School of Basic Medical Sciences, Xi'an Jiaotong University Health Science Center, No. 76 West Yanta Road, Xi'an, Shaanxi 710061, China.
E-mail address: zhangyixjtu@xjtu.edu.cn (Y. Zhang).
[1] These authors contributed equally to this work.

https://doi.org/10.1016/j.redox.2023.102944
Received 10 October 2023; Received in revised form 19 October 2023; Accepted 19 October 2023
Available online 21 October 2023

Nonstandard abbreviations and acronyms

VCAM-1	vascular cell adhesion molecule-1
ICAM-1	intercellular cell adhesion molecule-1
OSS	oscillatory shear stress
ECs	endothelial cells
MCECs	mouse coronary endothelial cells
HUVECs	human umbilical vein endothelial cells
VSMCs	smooth muscle cells
TAC	transverse aortic constriction
CAD	coronary artery disease
LCA	left coronary artery
ER	endoplasmic reticulum
RTN4	reticulon 4
MAMs	mitochondria associated ER membranes
ROS	reactive oxygen species
FS	fractional shortening
LVDd	left ventricular end-diastolic dimension
LVDs	left ventricular end-systolic dimension
MCU	mitochondrial calcium uniporter
VDAC1	voltage dependent anion channel 1
OPA1	OPA1 mitochondrial dynamin like GTPase
Mfn1	mitofusin 1
Mfn2	mitofusin 2
Drp1	dynamin related protein 1
Fis1	fission, mitochondrial 1

state at the lesion-prone regions of coronary arterial tree leading to CAD [4,8]. Overproduction of reactive oxygen species (ROS) may serve as an important common mechanism for the effect of these risk factors by upregulating adhesion molecules thereto promoting arterial intima inflammation [4,7,9,10]. In view of the close relevance of endothelial dysfunction for CAD, it is of great significance to further understand the pathological signaling and to identify key regulatory molecules.

Being an ER-residential protein, Reticulon-4 (RTN4) maintains the tubular ER structure [11]. ER and mitochondria are two highly interconnected organelles with the connecting sites known as mitochondrial-associated membranes (MAMs), and RTN4 were recently shown to also regulate the ER-mitochondria connection complex thereto affecting mitochondrial morphology and function in multiple cell types [12–15]. Among the three isoforms of RTN4, only Nogo-B is highly expresses in vascular cells, including smooth muscle cells (VSMCs) and endothelial cells (ECs), and acts as an important regulator of vascular homeostasis and remodeling [16]. Earlier clinical studies reported upregulation of Nogo-B in ECs in human carotid atherosclerotic plaques [17,18], suggesting participation of Nogo-B in this pathological process albeit the mechanism remains unidentified. Indeed, endothelial Nogo-B has been regarded as a component of the adhesion-induced pro-inflammatory signaling in ECs [19]. We previously showed a remarkable upregulation of Nogo-B expression in ECs upon inflammatory stimuli of ECs or in wild-type mice subjected to hypertension or pressure-overload with exacerbated cardiac hypertrophy [20,21]. Besides, Nogo-B was also shown to modulate the structure and function of mitochondria, one of the major sources of ROS, by controlling the ER-mitochondrial communications [12].

In this study, we hypothesized that under conditions of pressure-overload and hypercholesterolemia, Nogo-B orchestrates inflammatory processes in ECs via promoting mitochondrial ROS production and hence atheroprone endothelial dysfunction. To verify this, we firstly demonstrated the relationship between endothelial Nogo-B expression and the development of coronary atherosclerotic lesion in ApoE$^{-/-}$ mice subjected to transverse aortic constriction (TAC) surgery. Then, using cultured ECs under pro-inflammatory stimuli to simulate *in vivo* conditions, we assessed the role of Nogo-B in mitochondrial oxidative stress, intracellular inflammatory signaling, and expressions of adhesion molecules. Our results support a novel notion of Nogo-B in promoting endothelial dysfunction and coronary atherosclerosis under conditions of hypertension and hypercholesterolemia.

2. Methods

2.1. Animals

Apolipoprotein E deficient mice (ApoE$^{-/-}$) were purchased from Jackson Laboratory (Strain No:002052), which were then crossed with Nogo deficient (Nogo-A/B$^{-/-}$) mice (Strain No: T004776, GemPharmatech, Nanjing, China) to generate Nogo-A/B$^{-/-}$- ApoE$^{-/-}$ double knockout (DKO) mice. Nogo-A/B/C floxed mice (Nogo $^{f/f}$) obtained from Jackson Laboratory (Strain No: 033364) were crossed with VE-cadherin-Cre-ER^{T2} mice (Shanghai Model Organisms, Cat No: NM-KI-200173) [22] to generate EC-specific Nogo-B (the only isoform of Nogo expressed in ECs) knockout mice (Nogo-B^{ECKO}) [23], that were then crossed with ApoE$^{-/-}$ mice to generate Nogo-B^{ECKO}-ApoE$^{-/-}$ mice. To activate the Cre recombinase, mice (8 weeks of age) were intraperitoneally injected with tamoxifen (24 mg/kg/day, #T5648, Sigma-Aldrich) for 5 consecutive days. All strains were in the C57BL/6J background. Animals were housed in a pathogen-free environment under a 12 h/12 h light-dark cycle and fed a rodent diet ad libitum. Only Male mice were used in the experiments to avoid the possible impact of estrogen in atherosclerotic cardiovascular diseases in female [24]. Paraffin sections of coronary arteries in Beagle dog were purchased from Beijing SINOGENE Biotechnology Co., Ltd. All protocols and experimental procedures were approved by the Institutional Animal Care and Use Committee of Xi'an Jiaotong University and conformed to the Guide for the Care and Use of Laboratory Animals published by the National Institutes of Health.

2.2. Minimally invasive surgery for transverse aortic constriction

Mice (8–10 weeks of age) were subjected to TAC or sham operation as previously reported [20]. Briefly, Mice were anesthetized with isoflurane (2% for induction, 1.5% for maintenance). After hair removal, a horizontal incision of 0.5–0.8 cm in length was made at the level of second intercostal space. After retracting the thymus, the aortic arch was visualized using a dissecting scope (Motic SMZ-171). A 7-0 nylon ligature was tied between the innominate and left common carotid arteries with an overlying probe made from 27-gauge needle, which was then rapidly removed, leaving a discrete region of stenosis. Sham-operated animals underwent the same surgical procedure without the ligation of the aorta. After surgery, mice were intraperitoneally injected with buprenorphine hydrochloride (0.1 mg/kg) every 12 h for three days and carprofen (5 mg/kg) every 12 h twice. After *in vivo* study, mice were sacrificed with CO_2 in advance, and hearts were immediately collected and randomly divided for different assays in further experiments.

2.3. Treatment of test reagents in vivo

ApoE$^{-/-}$ and DKO mice were received injection of antioxidant N-Acetylcysteine (NAC, HY-B0215, 250 mg/kg in 100 μL saline/dose i.p.) or anti-TNFα antibody infliximab (IFX, HY-P9970, 10 μg/g in 100 μL saline/dose i.p.). Drugs were administered after completion of TAC surgery and animals were used to perform next experiments after 24 h.

2.4. Echocardiography

Cardiac dimensions and function were analyzed by transthoracic echocardiography using a Vevo 2100 system (VisualSonics Inc., Toronto, Canada) as previously described [25]. After removing hair on the chest, mice were anesthetized with isoflurane (2% for induction and 1.5% for maintenance), and the body temperature was kept at 37 °C. M-mode images were used to measure anterior and posterior LV wall thickness and internal diameters in end-systole and end-diastole (LVDs, LVDd), and fractional shortening (FS) was calculated as follows: [(LVDd-LVDs)/LVDd] × 100%. All measurements were obtained from images of 3–5 consecutive cardiac cycles, and the averages were used for analysis.

2.5. Cryostat histology and Oil Red O staining

After 7 weeks of TAC, hearts from ApoE$^{-/-}$, DKO mice and Nogo$^{f/f}$ ApoE$^{-/-}$, Nogo-B^{ECKO}-ApoE$^{-/-}$ mice were harvested, then rapidly fixed in 4% paraformaldehyde (PFA) overnight at 4 °C. PFA-fixed hearts were divided into 3 parts (base, medium, and apex), then incubated for 24 h in 30% sucrose solution at 4 °C on rotation, finally embedded in OCT. The whole heart was sectioned, with sets of 10 consecutive sections of 10 μm collected every 100 μm, then stored at −20 °C and performed the following staining experiments.

Serial transverse sections from one heart were cut from the aortic root to the apex with intervals of 200 μm. Sections were stained with Oil Red O. In brief, after washing in PBS, heart cryosections stained with 0.2% Oil Red O in 60% isopropanol for 10 min, and washed with 60% isopropanol for 1 min. After co-staining with hematoxylin, sections were washed and coverslipped with aqueous mounting medium. Images were captured by Olympus Image Pro Plus6 (Media Cybergenetics) microscope, and the area of Oil Red O staining was calculated using Image Pro Plus 6.0 software. The area of lumen (AL) and the area of plaque (AP) were measured and the ratio of AP/AL% calculated as the index of coronary stenosis. All measurements were performed in a blinded fashion.

2.6. Histopathological classification of coronary plaque phenotype

Referring to the pathological classification of human atherosclerotic plaques and the phenotype of mice plaque within the aortic roots [26], coronary artery atherosclerotic plaques of mice were sorted into 4 phenotypes as followings: (I) Intimal fatty streak: only a few oil red staining positive lipid droplets deposited in the inner wall of coronary vessels; (II) Intimal thickening: a small amount (<20% of the vascular lumen area) of plaque deposition in the inner wall of coronary vessels, with oil red staining positive lipid droplet deposition inside the plaque; (III) Fibrouscap atheroma: obvious fibrous cap in the plaque deposited in the inner wall of the coronary vessels; and (IV) Complex plaque: a massive oil red positive stained plaque (>80% of the vascular lumen area) deposits in the arterial vascular lumen, with secondary changes such as plaque rupture or calcification.

2.7. Immunofluorescence staining

Frozen heart sections were air dried at room temperature for 10 min, rinsed in PBS, incubated in 0.1% Triton X-100 in 5% BSA solution for 1 h at 37 °C, then co-stained overnight in 5% BSA solution at 4 °C with addition of antibodies against Nogo-A/B (1:200, cat#ab47085, Abcam), VE-cadherin (1:100, cat#sc-9989, Santa Cruz Biotechnology), αSMA (1:100, cat#67735-1-Ig, Proteintech) or CD68 (1:100, cat#MA513324, Thermo fisher), respectively. Slides were rinsed with PBS and then incubated with secondary antibodies (Alexa 488-labeled anti-mouse or Alexa 543-labeled anti-rabbit) in PBS for 1 h at room temperature. DAPI (1:10000, cat#62248, Thermo fisher) was used to stain nuclei.

Human umbilical vascular endothelial cells (HUVECs) were cultured on 25 × 25 mm glass microscope slides, fixed by 4% PFA for 10min, then co-stained overnight at 4 °C with antibodies against Nogo (1:200, cat#sc-271878, Santa Cruz Biotechnology) or COXIV (1:100, cat#4850, CST) in 5% BSA solution. Confocal immunofluorescence images were captured with Leica TCS SP8 STED 3X confocal microscopy. Analysis of the aspect ratio and number of mitochondria was performed in Image Pro Plus 6.0 software.

2.8. Transmission electron microscopy

Transmission electron microscopy (TEM) was used to observe the ultrastructure of mouse cardiac ECs. In brief, fresh tissue blocks (1 mm^3) were immediately fixed with 2.5% glutaraldehyde. After fixation, the samples were dehydrated in a graded ethanol series and embedded in acrylic resin (LR White). The blocks were cut into sections (50–70 nm) using LKB-V/Leica UC7 ultramicrotome (LKB-V/NOVA, Sweden and Leica, Germany). Samples were observed in the transmission electron microscope (Hitachi Model H-7650). For ER-mitochondrial distance and mitochondrial number quantification, images were randomly obtained at magnifications of ×4000 and ×10,000, respectively (over 15 images for each magnification per sample). Analysis of the ER-Mito distance was performed in ImageJ software in a blinded fashion.

2.9. Preparation of primary mouse heart endothelial cells

Primary mouse coronary endothelial cells (MCECs) were isolated from male ApoE$^{-/-}$ mice or DKO mice at 10 weeks of age and cultured as previously described [22]. MCECs were cultured in DMEM with antibiotics and 10% FBS for 7 days, then harvested for evaluating protein expressions between ApoE$^{-/-}$ and DKO hearts followed by Western blotting.

2.10. Cell culture and siRNA interference

HUVECs were cultured in M199 medium supplemented with antibiotics and 10% FBS. When grown to approximately 70% confluence, cells were transfected with control or siRNAs. Specific siRNAs (5 nM) for silencing the Nogo-B and NgBR gene were synthesized by Gene Pharma Company (Shanghai, China). Transfection was accomplished using Lipofectamine™ RNAimax (ThermoFisher, cat#13778030) according to manufacturer's protocols with the following siRNA sequences:

Nogo-B-siRNA:
sense: 5′-GUGUUGAUGUGGGUAUUUATT-3′,
antisense: 5′-UAAAUACCCACAUCAACACTT-3'.
NgBR-siRNA:
sense: 5′- GUUAGCCAGUUUACUUAGUT -3′,
antisense: 5′- ACUAAGUAAACUGGCUAACTT -3'.

Expression levels of Nogo-B and NgBR were assessed between 48 h post-transfection by Western blotting.

2.11. Oscillation shear stress

HUVECs were seeded on specific glass slides accommodated to flow chamber. When cell density on the slides reached about 80%, cells were starved in the FBS-free medium for 6 h, and then assembled to fluid shear stress system (Ibidi GmbH, Germany) and applied 4 dyn/cm^2 OSS for 24 h (with the untreated static chambers served as control). The flow chamber was maintained a constant temperature at 37 °C with 5% CO_2 in air during the experiment. Quantitative PCR or immunofluorescence staining were performed to measure the expression level of Nogo-B and VCAM-1 after applying 24-h OSS.

2.12. Live cell calcium imaging

HUVECs were seeded on 25 × 25 mm glass microscope slides in 6-well plates, and transfected with control or Nogo-B-siRNA for 48 h.

For real-time imaging of Ca^{2+} level of cytoplasm, cells were loaded with 5 μM Fura-2AM (F1221, Invitrogen™) for 30 min at 37 °C in Tyrode solution containing (in mM): NaCl 137, glucose 12, HEPES 20, KCl 5.4, $MgCl_2$ 1.2, NaH_2PO_4 1.2, and $CaCl_2$ 1.8, adjusted to pH 7.4. Cells were then washed three times and stimulated by histamine (10 μM) or ATP (10 μM), Ca^{2+} transient was measured by a high-speed cooled CCD camera (C9100, Hamamatsu, Japan) at a speed of 10 frames per s (fps) as previously described [27]. For real-time imaging of mitochondrial Ca^{2+} level, cells were loaded with 5 μM Rhod-2 AM (R1244, Invitrogen™) for 20 min at room temperature in Tyrode solution, then Ca^{2+} transient of the cells stimulated by histamine (10 μM) or ATP (10 μM) was measured by Leica TCS SP8 STED 3X confocal microscopy.

2.13. Intracellular and mitochondrial oxidative stress detection

The intracellular ROS level of HUVECs were tested with CM-H_2DCFDA (DCF, C6827, Invitrogen™) fluorescent staining. Cells were loaded with 5 μM DCF for 30 min at room temperature in Tyrode solution. After washing out, DCF fluorescent images were acquired with a Leica TCS SP8 STED 3X confocal microscopy equipped with 40 × , 1.3 NA oil immersion objective (excitation 488 nm, emission 495–550 nm) with fixed scanning parameters. The specificity of ROS detection by DCF was checked by 10 min treatment of 0.3% H_2O_2 as positive control and 5 mM NAC preincubation as negative control, and unstained cells as background (Fig. S1). The mean intensity of DCF fluorescence were analyzed by ImageJ software.

For mitochondrial oxidative stress detection, HUVECs were incubated for 20 min at 37 °C with 5 μM MitoSOX Red (M36008, Thermo-Fisher Scientific) and washed. Then cells were collected for flow cytometric analysis of MitoSOX Red fluorescence intensity. The 1×10^4 live cells in each sample were quantified by flow cytometer (BD FACS Celesta). The specificity of mitochondrial ROS detection with MitoSOX Red staining was checked by preincubation with 20 μM MitoTEMPO as negative control and unstained images as background (Fig. S2). The data from flow cytometry were analyzed using FlowJo software, and mean fluorescence intensity (MFI) in each group was calculated.

2.14. HPLC analysis of DHE oxidative products

Intracellular ROS was assessed with the specific 2-hydroxyethidium and non-specific ethidium products of dihydroethidium (DHE) oxidation as previously described [28]. HUVECs were treated with 10 μM DHE (D11347, Invitrogen™) for 30 min in HBSS, then washed with HBSS twice and lysed with methanol. Supernatants were collected after centrifuged at 12,000 g for 15 min. Samples (20 μL) were injected into the HPLC system (UltiMate 3000, Thermo Fisher, USA) with a C18 column (250 × 4.6 mm) and monitored with a fluorescence detector (Ex/Em = 510/580 nm). Mobile phase A was 0.1% trifluoroacetic acid in H_2O, and mobile phase B was 0.1% trifluoroacetic acid in acetonitrile. 2-Hydroxyethidium products were separated using a gradient of acidified acetonitrile/water mixture (from initial 90%/10% mobile phase A/B to 30%/70% in 40 min, and then reaching the initial 90%/10% in 5 min). The flow rate was maintained at 0.5 ml/min.

2.15. Cytokine array analysis

Plasma from $ApoE^{-/-}$ and DKO mice underwent 24 h-TAC were collected and used to determine levels of 20 mouse cytokines including GM-CSF, IFN-gamma, IL-1α, IL-1β, IL-10, IL-12 p70, IL-13, IL-17A, IL-2, IL-3, IL-4, IL-5, IL-6, IL-9, KC (CXCL1), MCP-1 (CCL2), M-CSF, RANTES (CCL5), TNFα and VEGF-A using Quantibody Mouse Cytokine Array 1 (QAM-CYT-1, RayBiotech, Norcross, GA, USA) according to the manufacturer's instruction.

2.16. Western blotting

Western blotting was performed as previously reported [25]. Polyvinylidene fluoride membranes were incubated at 4 °C overnight using the following antibodies: Nogo-A/B (1:2000, #ab47085, Abcam); VCAM-1 (1:2000, #T55427, Abmart); ICAM-1 (1:500, #T40024, Abmart); P38 (1:1000, #9212, CST); p-P38 (1:1000, #9216, CST); P65 (1:1000, #8242, CST); p-P65 (1:1000, #3033, CST); AKT (1:1000, #9272, CST); P-AKT (1:1000, #9271, CST); IP3R1 (1:500, #ACC-019, Alomone); NgBR (1:1000, #TN25175S, Abmart); NOX2 (1:1000, #19013-1-AP, proteintech); NOX1 (1:1000, #17772-1-AP, Proteintech); NOX4 (1:1000, #14347-1-AP, proteintech); OPA1 (1:1000, #67589, CST); Drp1 (1:1000, #5391, CST); Mfn1 (1:1000, #66776-1-Ig, proteintech); Mfn2 (1:1000, #12186-1-AP, proteintech); VDAC1 (1:2000, #66345-1-Ig, proteintech); MCU(1:2000, #26312-1-AP, proteintech); Fis1(1:500, #10956-1-AP, proteintech) and GAPDH (1:5000, #HRP-60004, proteintech), followed by the rabbit or mouse with HRP-conjugated secondary antibody. All immunoblotting bands were developed using an enhanced chemiluminescence detection system (Bio-Rad, Hercules, CA) and quantified using ImageJ software.

2.17. Co-immunoprecipitation

Co-immunoprecipitation experiments were performed as previously described [29]. Briefly, protein was extracted from HUVECs using NP40 lysis buffer cocktails (cat#P0013F, Beyotime, Shanghai, China). The lysate was immunoprecipitated with anti-Nogo antibody (cat#T57213, Abmart) or anti-Mfn2 antibody (cat#12186-1-AP, proteintech) at 4 °C overnight, followed by incubation at 4 °C for 2 h with protein A/G agarose beads (cat#sc-2003, Santa Cruz, CA, USA). The beads were washed over three times with lysis buffer cocktails. Immunoprecipitates were boiled in SDS-loading buffer and analyzed by Western blotting using anti-Mfn2 antibody or anti-Nogo antibody.

2.18. Statistics

Data are expressed as mean ± SD. GraphPad Prism software (v7.0 and v9.0 GraphPad Software, San Diego, CA) was used for all statistical analyses. After the assumptions of normality and equal variances were assessed by Shapiro-Wilk and Brown-Forsythe tests, respectively, non-parametric test (for non-normally distributed variables), or student's *t*-test (for 2 groups of normally distributed variables)/one-way or two-way ANOVA (for three or more groups of normally distributed variables) with Tukey's multiple comparisons post hoc tests were used for all statistical analyses. Differences were considered statistically significant at $P < 0.05$. All tests were two-sided.

3. Results

3.1. Deficiency of Nogo-B alleviated LCA atherosclerotic lesion in $ApoE^{-/-}$ mouse hearts subjected to chronic TAC

Previous studies showed highly expressed Nogo-B in ECs from neovascularized areas in the human carotid plaques [18]. To investigate the role of Nogo-B in the formation of coronary atherosclerotic lesion, we generated and studied $ApoE^{-/-}$ and Nogo-A/$B^{-/-}$-$ApoE^{-/-}$ (DKO) mice. While Nogo-B was present in majority of cells within and around the plaque, upregulated expression of Nogo-B was mostly co-localized with the endothelium (marked by VEC) in mouse hearts (Fig. 1A and B, Fig. S3). Elevated Nogo-B expression was consistently observed in heart tissues from $ApoE^{-/-}$ mice subjected to 24-h, 72-h, or 7-week TAC, which was abolished in DKO mice (Fig. 1C–E). Nogo-B upregulation was also similarly observed in canine hearts with atherosclerotic plaques due to ApoE deletion (Fig. S4).

We previously established a mouse model of coronary atherosclerosis in chow diet-fed $ApoE^{-/-}$ mice subjected to TAC [30]. Consistent to our

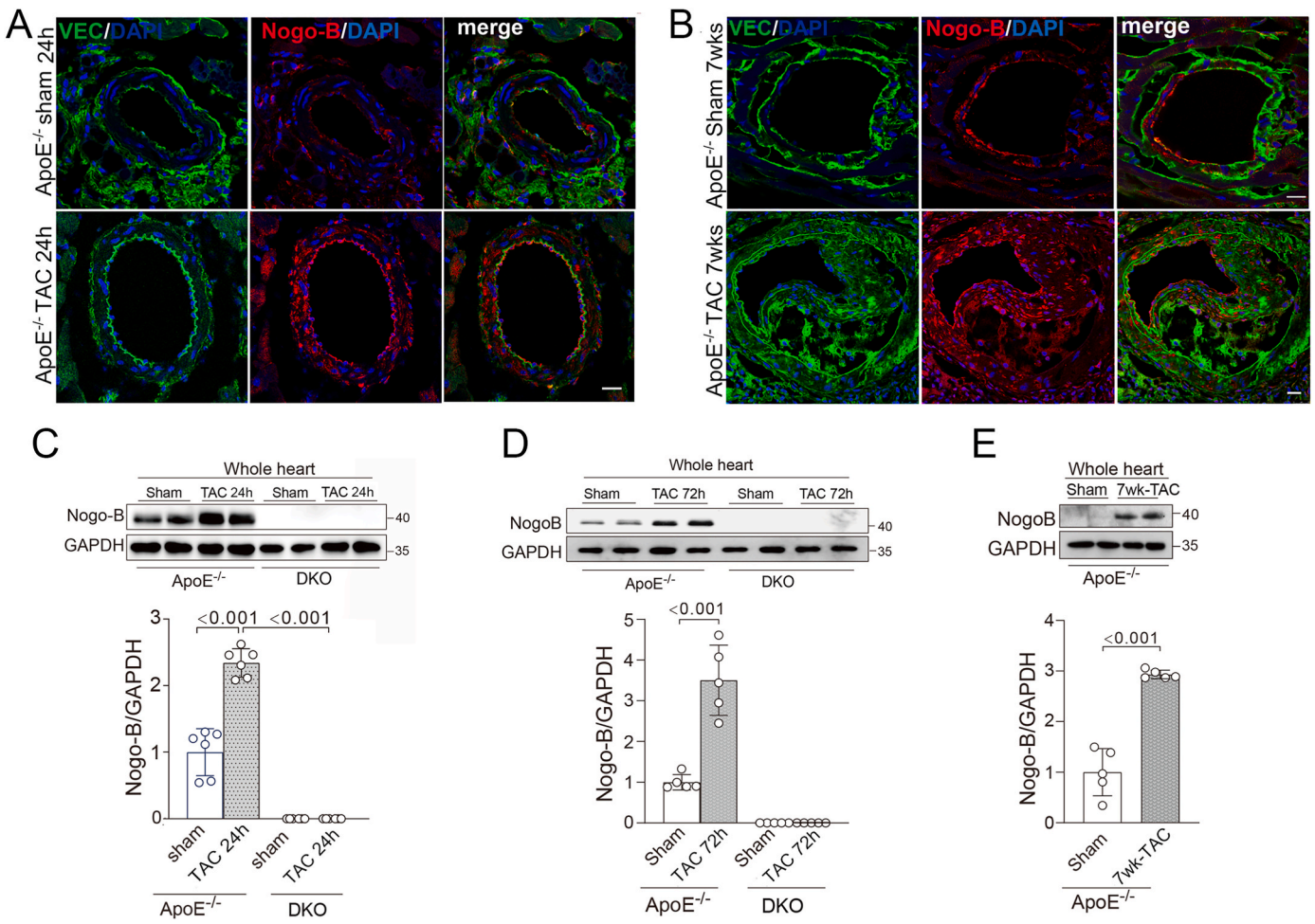

Fig. 1. Nogo-B upregulated in heart tissues of ApoE$^{-/-}$ mice after TAC. (**A**) Immunofluorescence staining of heart sections with Nogo-B (red), endothelial cell marker VE-cadherin (VEC, green) and nuclei DAPI, from ApoE$^{-/-}$ mice after 24-h or (**B**) 7 weeks TAC. Scale bar: 20 μm. (**C**–**E**) Representative Western blotting images and quantifications of protein levels of Nogo-B in whole heart tissues from ApoE$^{-/-}$ and Nogo-A/B$^{-/-}$ApoE$^{-/-}$ (DKO) mice subject to 24-h (**C**), or 72-h (**D**), or 7-week (**E**) sham and TAC operation. n ≥ 5 mice/group. P value with statistical significance were labeled above the connected lines between indicated groups (one-way ANOVA with Tukey's multiple comparisons test). (For interpretation of the references to colour in this figure legend, the reader is referred to the Web version of this article.)

prior findings, ApoE$^{-/-}$ mice with chow diet developed cardiac hypertrophy with reduced LV function, markedly lipid deposition in the left coronary artery (LCA) and even myocardial infarction after 7 weeks of TAC (Fig. 2A and B, Fig. S5). Compared to ApoE$^{-/-}$group, DKO mice subjected to the same treatment had better persevered cardiac function and absence of recognizable lipid deposition in the LCA (Fig. 2A). Oil Red O staining of sequential heart sections revealed decreased LCA plaque area at each section along the axis of the aortic root to the apex in DKO versus ApoE$^{-/-}$ hearts of mice with TAC (Fig. 2C–F). Furthermore, according to the histopathological classification of coronary plaque phenotypes (intimal fatty streak, pathological intimal thickening, fibrous cap atheroma and complicated plaque), at 7 weeks of TAC, the lipid deposition plaque in DKO mouse hearts were mostly in the first two stages, whilst the more advanced phenotypes of coronary plaque were common in ApoE$^{-/-}$ counterparts (Fig. 2E).

We then measured the necrotic core and fibrous cap thickness known to be associated with plaque instability and rupture [31]. We firstly observed presence of fibrotic patches by Masson's and αSMA staining indicating small infarcts of the LV owing to myocardial ischemia due to coronary plaques (Fig. 2G). As shown in Fig. 2H–J, the DAPI-negative necrotic areas inside the plaques were significantly reduced. And fibrous cap thickness, quantified with the αSMA^{+} area around the necrotic core of the plaques, was significantly greater in DKO versus ApoE$^{-/-}$ hearts. These findings indicate that Nogo-B deficiency stabilized the coronary plaque in ApoE$^{-/-}$ mouse hearts post TAC.

Unlike the remarkable hypercholesterolemia in 5-week HFD feed ApoE$^{-/-}$ mice, the plasma cholesterol levels in both TAC-operated ApoE$^{-/-}$ and DKO mice were much lower and comparable (Fig. S6). Furthermore, plasma levels of angiotensin II were comparable between ApoE$^{-/-}$ and DKO groups (Fig. S7). Thus, the distinct plaque phenotypes in TAC-operated ApoE$^{-/-}$ and DKO mice could not be attributable to differences in either cholesterol or angiotensin II.

3.2. *Nogo-B mediated the upregulation of adhesion molecules in endothelial cells upon oscillatory shear stress or inflammatory stimuli*

Under stressed conditions like hypertension, upregulation of adhesion molecules (VCAM-1/ICAM-1) is an important indication of endothelial dysfunction predicting future cardiovascular risks [32]. We then evaluate whether Nogo-B expression correlated with the level of VCAM-1 in ECs under pathological stimuli. In HUVECs under 24-h oscillatory shear stress (OSS) stimulation mimicking hypertensive conditions *in vivo*, protein expression of both VCAM-1 and Nogo-B was significantly increased indicated by immunofluorescence staining (Fig. 3A and B), quantitative mRNA expressions (Fig. 3C), or Western blot analysis of the whole heart lysate. At 24 h post TAC, VCAM-1

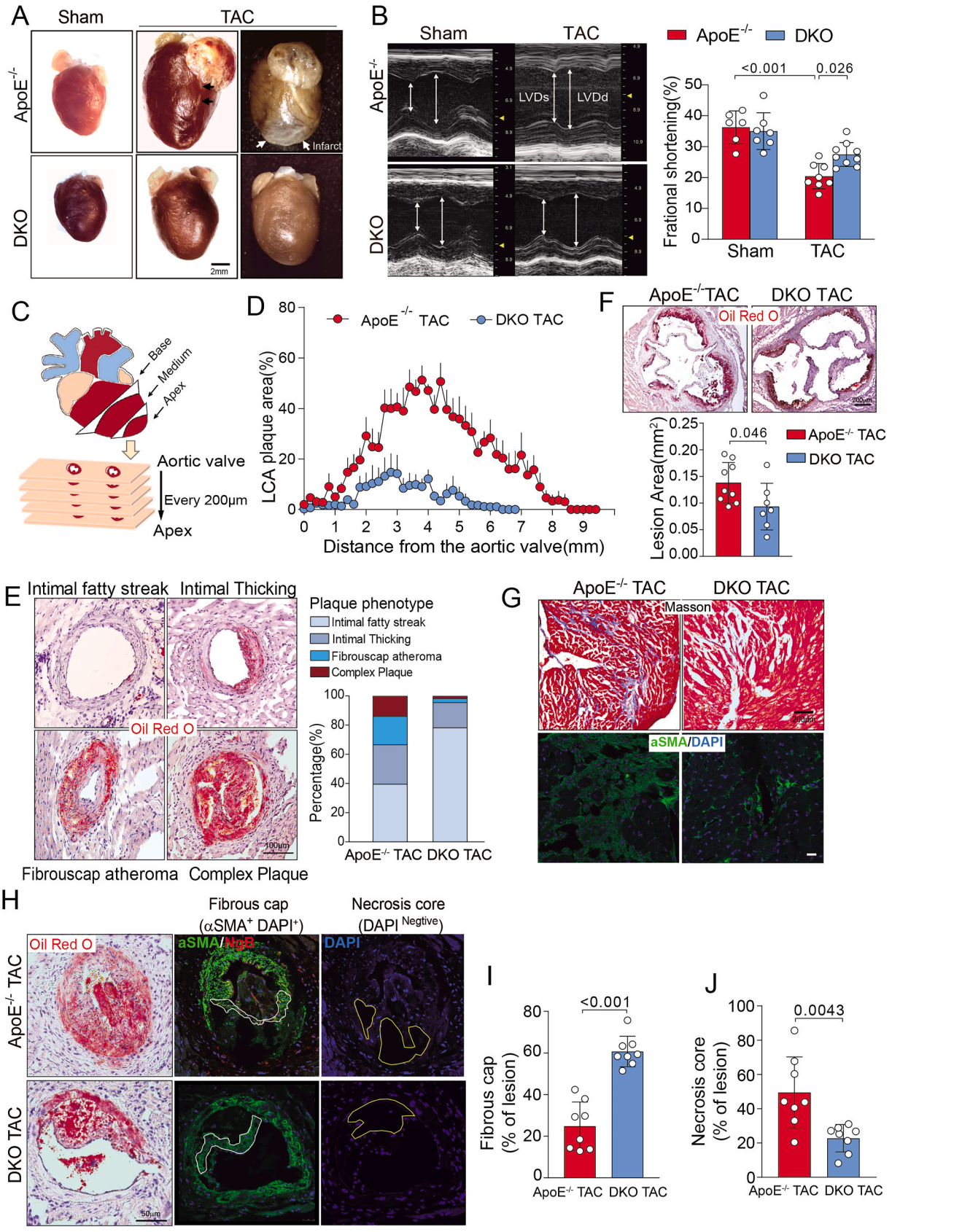

(caption on next page)

Fig. 2. Deficiency of Nogo-B alleviated LCA atherosclerotic lesion in ApoE$^{-/-}$ mice subjected to TAC for 7 weeks. (**A**) Representative images of hearts from sham- and 7-week TAC-operated ApoE$^{-/-}$ and Nogo-A/B$^{-/-}$ApoE$^{-/-}$ (DKO) mice. The black arrows indicate the lipid deposition in LCA (middle) and the white arrows indicated the infarct area (right). Scale bar: 2 mm. (**B**) Representative M-mode echocardiographic images and LV fractional shortening (FS) at each group (n ≥ 6 mice/group). (**C**) Schematic plot showing sequential sectioning of hearts at every 200 μm, and (**D**) statistics of LCA plaque areas in each section alongside aortic valve to apex in TAC mice (n = 7 hearts/group). (**E**) Representative Oil Red O-staining lipid deposition images (left) and distribution (right) of LCA plaque phenotypes calculated from each section alongside aortic valve to apex in hearts from mice with TAC. n = 7 mice/group. (**F**) Representative Oil Red O staining images and the quantification of plaque size at aortic roots of mice post TAC. Scale bar: 200 μm. n ≥ 7 mice/group. (**G**) Cardiac interstitial or patch fibrosis identified by Masson's trichome staining (upper) or αSMA (green)/DAPI (blue) immunofluorescence staining (lower). Scale bar: 20 μm. (**H**) Representative immunofluorescence images and quantification of (**I**) αSMA positive fibrous cap (white box indicated) and (**J**) DAPI negatively stained necrotic core (yellow box indicated) in LCA plaques of mouse hearts 7 weeks post-TAC (n = 8 mice/group). (For interpretation of the references to colour in this figure legend, the reader is referred to the Web version of this article.)

protein level increased by about 3-fold in ApoE$^{-/-}$mice compared to sham group. These changes were abolished in DKO mice (Fig. 3D).

It has been suggested that expression of inflammatory cytokines were *de novo* induced following cardiac pressure overload [33]. After 24-h TAC, plasma levels of multiple inflammatory cytokines, including TNFα and IL-1β, were elevated in ApoE$^{-/-}$ mice, which were partially rescued with Nogo-B deletion (Fig. 3E, Fig. S8). We then evaluate whether Nogo-B expression correlated with the level of VCAM-1 in ECs. Upon 24-h TNFα stimulation, expression of both VCAM-1 and Nogo-B were significantly upregulated in MCECs, while deletion of Nogo-B in MCECs prevented VCAM-1 upregulation (Fig. 3F). Similarly, HUVECs subjected to TNFα or IL-1β stimuli displayed elevated expression of Nogo-B as well as VCAM-1/ICAM-1 in a concentration-dependent manner (Fig. 3G, Fig. S9).

3.3. ROS-p38-p65 signaling were involved in Nogo-B-associated upregulation of adhesion molecules in endothelial cells

After documenting the *in vivo* simulation of cultured ECs exposured to inflammatory cytokines, we then explored the pathway underlying Nogo-B mediated upregulation of adhesion molecules. Using cultured HUVECs stimulated with inflammatory cytokines mostly by TNFα, silencing Nogo-B with siRNAs eliminated TNFα-stimulated VCAM-1 upregulation (Fig. 4A). In order to clarify whether such causal role of Nogo-B in upregulating VCAM-1 required its interaction with membrane Nogo-B receptor (NgBR), we determined in HUVECs subjected to TNFα stimulation, and found that the expression of NgBR was unchanged by TNFα, and that siRNA interference of NgBR expression had no effect on TNFα-induced upregulation of VCAM-1 (Fig. 4B). These findings excluded the involvement of NgBR.

It has been well shown that the p38MAPK pathway participates in the induction of pro-inflammatory gene expression through p65 phosphorylation, particularly in the context of TNFα signaling [34]. We thus tested whether this pathway was coupled with Nogo-B. Upon TNFα stimulation, the phosphorylation levels of p38 (Thr180 and Tyr182 sites) and p65 (Ser536 site) reached the peak at 15 min, whereas the phosphorylated Akt showed no change (Fig. 4C, Fig. S10). Under diseased conditions, activation of p38 signaling has been associated with the intracellular oxidative stress [35,36]. Indeed, treatment of HUVECs with the ROS scavenger, N-acetyl-L-cysteine (NAC), significantly lowered TNFα-induced p38/p65 phosphorylation (Fig. 4D). Combination of Nogo-B siRNA knockdown and NAC treatment showed additive efficacy in reversing p38 activation (Fig. 4D).

Mitochondria is one of the major cellular sources for ROS production, which could amplify overall ROS generation from other sources like NADPH oxidases (NOX) through the mitochondrial ROS-induced ROS release [10,37]. We then evaluated the mitochondrial as well as intracellular ROS levels in HUVECs in the presence and absence of TNFα. By flow cytometry analysis-quantified mitochondria-residential MitoSOX Red fluorescence, TNFα stimulation for 24 h elevated mitochondrial oxidative stress in HUVECs, which was largely suppressed by silencing Nogo-B (Fig. 5A and B). After 24-h TNFα stimulation, the oxidative stress level in HUVECs was also significantly elevated as indicated by DCF fluorescence (Fig. 5C and D) or by HPLC analysis of DHE oxidative products (Fig. 5E and F). Meanwhile, the NOX activity and expression of NOX2, but not NOX1 and NOX4, in HUVECs were elevated by 24-h TNFα stimulation. Once again all these changes were abolished by silencing Nogo-B (Fig. 5G–H, Fig. S11).

We also assessed whether the ROS-p38-p65 axis was responsible for TNFα-induced VCAM-1 expression through Nogo-B signal hub. TNFα-induced VCAM-1 upregulation in HUVECs was suppressed by interferences of Nogo-B knockdown with siRNAs or by pre-treatment with several test agents including mitochondria-targeted antioxidant Mitotempo, the ROS scavenger N-acetyl-L-cysteine (NAC), NOX2 inhibitor GSK2795039, or SB203580 as inhibitor of p38 phosphorylation (Fig. 6A–C, Fig. S12).

To further confirm the role of pro-inflammatory ROS generation in atherosclerotic vessels, ApoE$^{-/-}$ and DKO mice were treated with NAC or a bolus of infliximab (a chimeric anti-TNFα monoclonal antibody) immediately after TAC surgery and animals were studied at 24 h afterwards. Both treatments attenuated upregulation of VCAM-1 in ApoE$^{-/-}$ mice (Fig. 6D and E).

3.4. Nogo-B maintained ER-mitochondria tethering by Mfn2 and the resultant Ca^{2+} transport in endothelial cells

As an ER-residential protein, Nogo-B has also been implicated as a member of MAM proteins participating in the regulation of mitochondrial morphology and function in VSMCs [14]. Whether and how Nogo-B regulated ER-mitochondrial function in ECs remain unknown. We then investigated the association between Nogo-B and mitochondrial morphology marker proteins (OPA1, Mfn1, Drp1, Fis1, and Mfn2). In MCECs isolated from DKO hearts, Mfn2 protein level was significantly lower without alteration in its mRNA level compared to ApoE$^{-/-}$ group, while alteration in other proteins was not observed (Fig. 7A, Fig. S13). In HUVECs overexpressed with Ad-Nogo-B, the expression of Mfn2 was doubled over the control group transfected with Ad-GFP (Fig. 7C and D). Furthermore, co-immunostaining revealed co-localization of Mfn2 and Nogo-B in condensed mitochondrial areas around nuclei (Fig. 7B). The physical interaction of Nogo-B and Mfn2 was further confirmed by co-immunoprecipitation (Fig. 7E).

Mfn2 has been proven to function as a tether, fastening the ER with the mitochondria outer membrane thereby maintaining an intact mitochondria-ER unit [38,39]. We then observed the ER-mitochondrial morphology in ECs of ApoE$^{-/-}$ and DKO mouse hearts by electron microscopy imaging. After 24 h aortic banding, the ER-mitochondrial distance in coronary ECs were obviously much greater with Nogo-B deletion (Fig. 7F and G).

Mitochondria uptake Ca^{2+} from adjacent ER to maintain their proper functions including ROS generation, ATP synthesis and so on. To test whether Nogo-B affected ER-mitochondrial Ca^{2+} transport, live-cell confocal microscopy was employed to simultaneously measure the cytosolic and mitochondrial Ca^{2+} signals in HUVECs transfected with si-Negative control (NC) or si-Nogo-B. Upon histamine or ATP-stimulated Ca^{2+} release from ER, while there was no difference in the peak of cytosolic Ca^{2+} transients between both groups, the mitochondrial Ca^{2+} uptake was significantly reduced in si-Nogo-B transfected cells (Fig. 7H and I). Such reduction on mitochondrial Ca^{2+} by Nogo-B deletion was

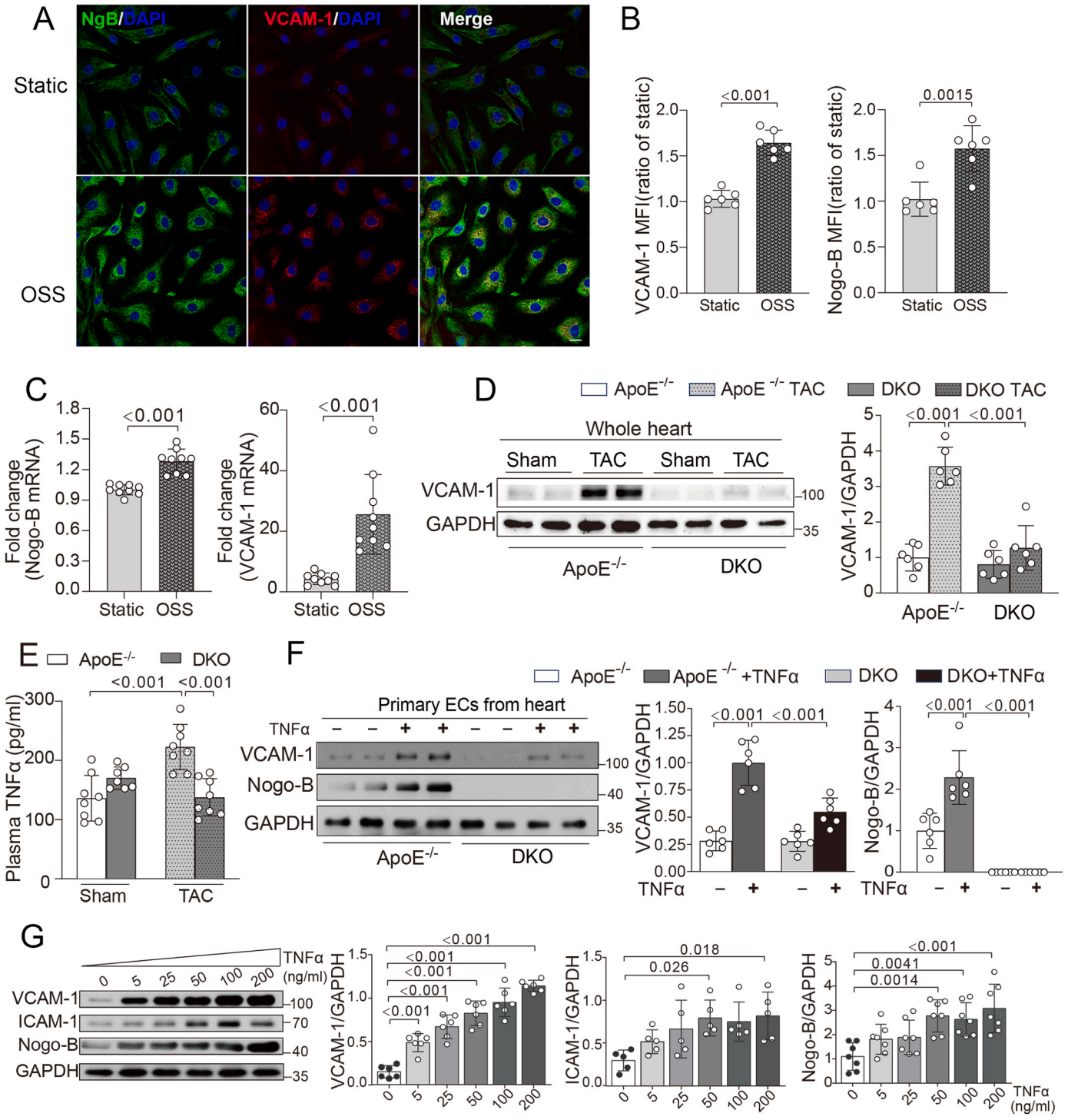

Fig. 3. Inflammatory stimuli or oscillatory shear stress (OSS) upregulated expression of endothelial Nogo-B and adhesion molecules. (**A**) Immunofluorescence staining of HUVECs with Nogo-B (green), VCAM-1 (red) and nuclei DAPI, from static or 24-h OSS stimulation. Scale bar: 20 μm. (**B**) Quantification of mean fluorescence intensity (MFI) of Nogo-B and VCAM-1 in static and 24-h OSS stimulation. n = 6 independent experiments for each group. (**C**) mRNA level of Nogo-B and VCAM-1 in HUVECs under static condition or 24-h OSS stimuli. n = 9 independent experiments for each group. (**D**) Representative Western blotting images and quantifications of protein levels of VCAM-1 in whole heart tissues from ApoE$^{-/-}$ and DKO mice of Sham or 24-h TAC operation. n = 6 mice/group. (**E**) Plasma TNFα levels from ApoE$^{-/-}$ and DKO mice 24-h post sham or TAC surgery, n ≥ 7 mice/group. (**F**) Representative Western blotting images and quantifications of protein levels of VCAM-1 or Nogo-B in MCECs prepared from ApoE$^{-/-}$ and DKO mice and treated with vehicle or TNFα for 24 h. n = 6 independent isolations. (**G**) Western blot analysis of VCAM-1, ICAM-1, and Nogo-B in HUVECs treated with concentrations (0–200 ng/ml, 24 h) of TNFα. n ≥ 5 independent experiments. (For interpretation of the references to colour in this figure legend, the reader is referred to the Web version of this article.)

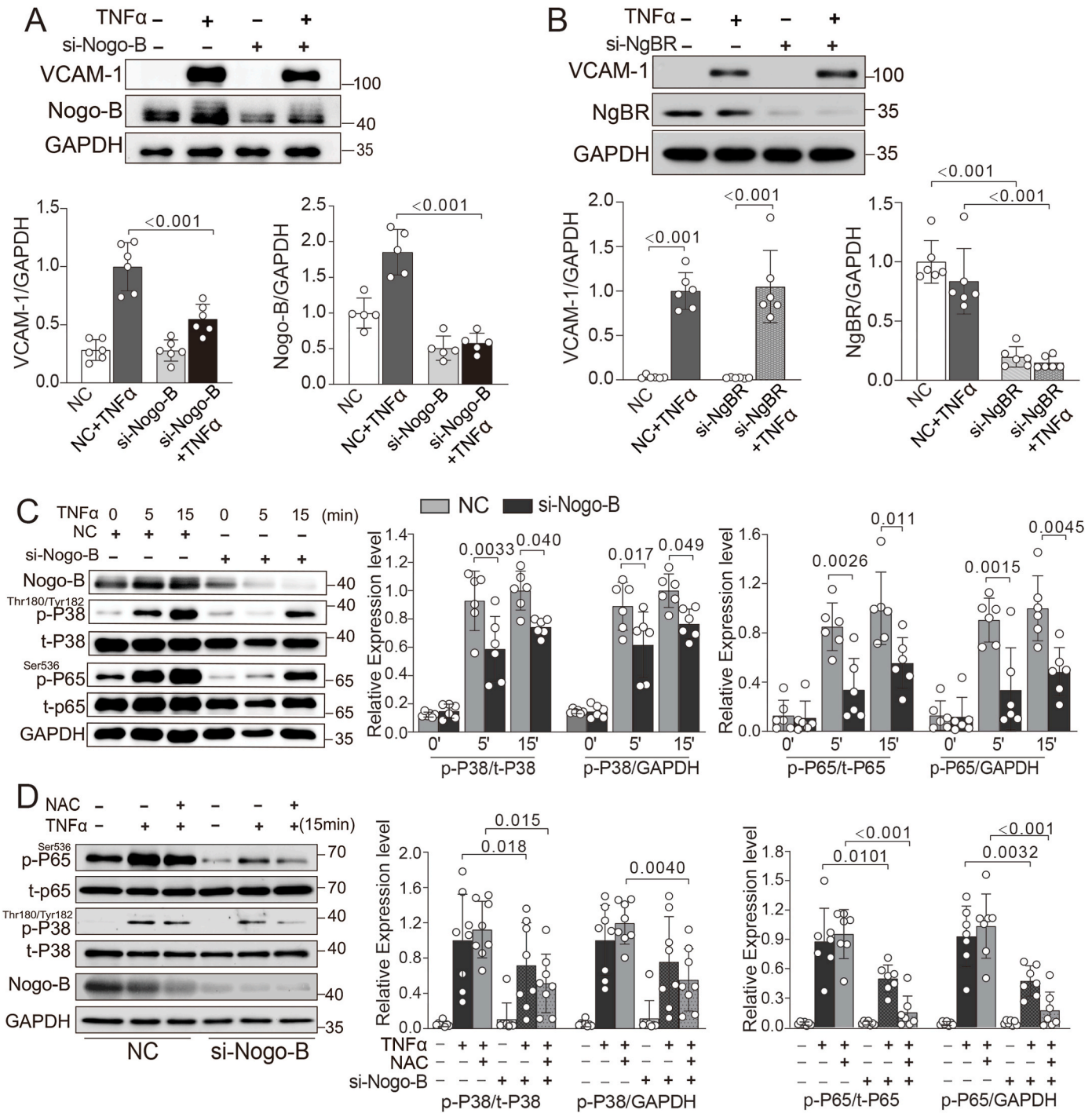

Fig. 4. Nogo-B augmented mitochondrial ROS production and subsequent activation of the p38-p65 pathway in HUVECs upon TNFα stimulation. Silencing Nogo-B in HUVECs with siRNAs eliminated the TNFα-stimulated VCAM-1 expression (**A**), but silencing NgBR had no effect on VCAM-1 expression (**B**). (**C**) Representative Western blotting images and quantifications of protein levels for total and phosphorylated p38 and p65 in HUVECs transfected with scrambled (NC) or Nogo-B siRNA (si-Nogo-B) under vehicle or TNFα (100 nM) stimuli for 0–15 min. (**D**) Western blot analysis of p38-p65 levels in HUVECs transfected with NC or si-Nogo-B and stimulated with TNFα in the presence or absence of NAC (5 mM). n ≥ 6 for each group.

closely associated with an increased ER-mitochondria distance. Such association might be causative given that there was no alteration on the expression levels of known marker proteins associated with ER-mitochondria Ca^{2+} transport (IP3R1, MCU, VDAC1) in MCECs isolated from ApoE$^{-/-}$ and DKO hearts (Fig. 7J–K, Fig. S14). We also showed that inhibition of ER Ca^{2+} release with the IP_3R inhibitor 2-APB (10 μM) prevented the upregulation of VCAM-1 and Nogo-B in HUVECs under 24-h TNFα exposure (Fig.7L).

3.5. *Endothelial Nogo-B mediated the formation of coronary plaque in ApoE$^{-/-}$ mouse hearts*

To further verify the influence of endothelial Nogo-B on the form of coronary plaque in ApoE$^{-/-}$ mouse hearts, we studied mice with the endothelial-specific Nogo-B inducible deletion (Nogo-B^{ECKO}) in the ApoE$^{-/-}$ background. Western blotting analysis of Nogo-B expression showed remarkable reduction of Nogo-B in whole heart lysate from

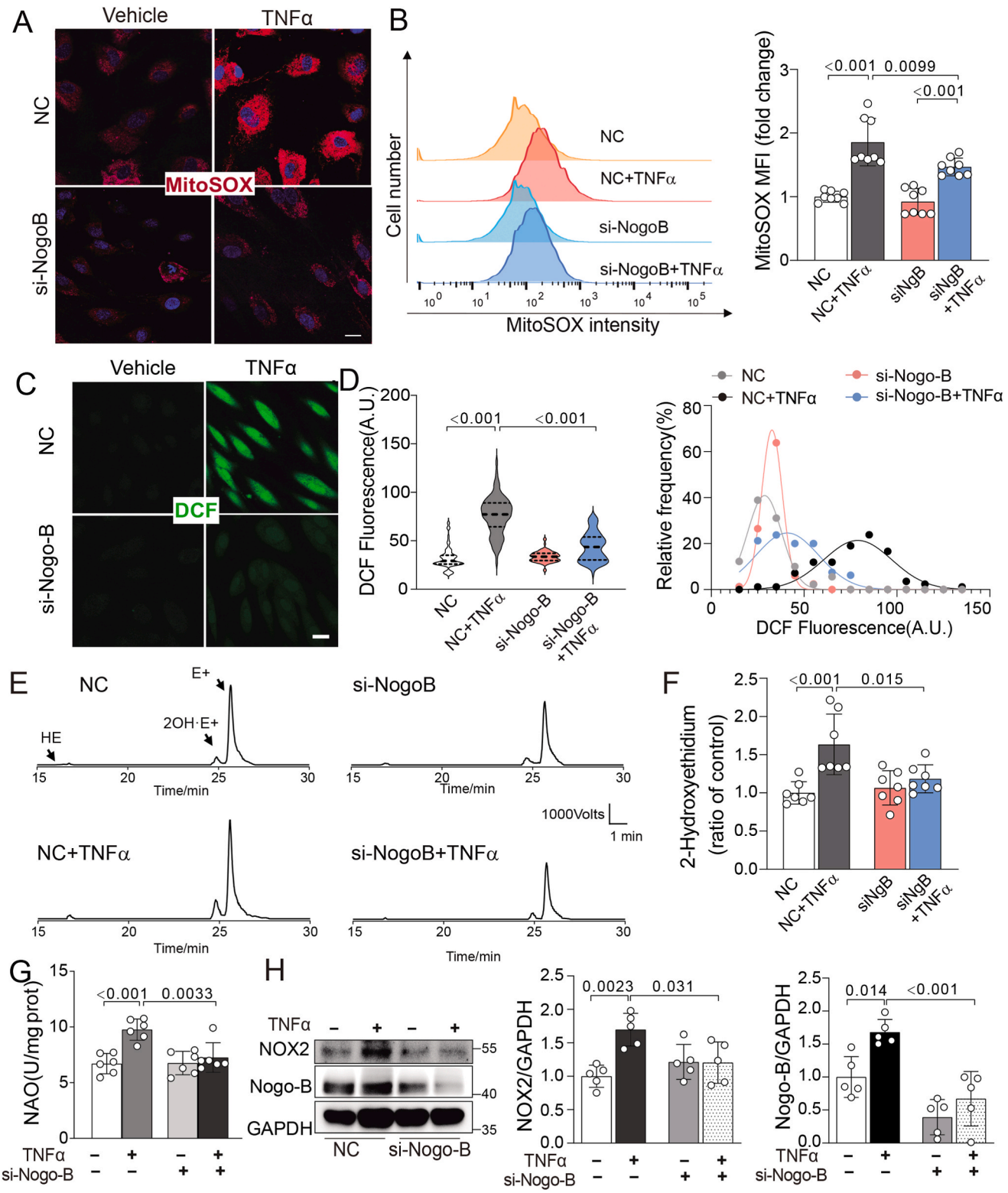

Fig. 5. Nogo-B mediated excess ROS production in HUVECs upon TNF-α stimulation. (**A**) Representative confocal images of MitoSOX Red fluorescence in HUVECs. (**B**) Flow cytometric analysis of MitoSOX Red staining-indicated mitochondrial ROS level and quantification by MFI from scrambled (NC) or Nogo-B siRNA under vehicle or TNFα stimuli for 24 h n = 8/group. (**C**) Representative images of DCF fluorescence and (**D**) Intensity statistics and distribution of DCF fluorescence images in HUVECs under 24-h TNFα stimulation. n ≥ 80 (DCF-DA Green) cells from 6 independent experiments. (**E**) representative traces and (**F**) statistics of HPLC analysis of DHE oxidative products in HUVECs lysates transfected with scrambled (NC) or Nogo-B siRNA under vehicle or TNFα stimuli for 24 h. n = 7 independent experiments for each group. (**G**) NOX activity assays in TNFα-stimulated HUVECs transfected with NC or si-Nogo-B. n = 5/group. (**H**) Western blot analysis of NOX2 in TNFα-stimulated HUVECs transfected with NC or si-Nogo-B. n = 5/group. (For interpretation of the references to colour in this figure legend, the reader is referred to the Web version of this article.)

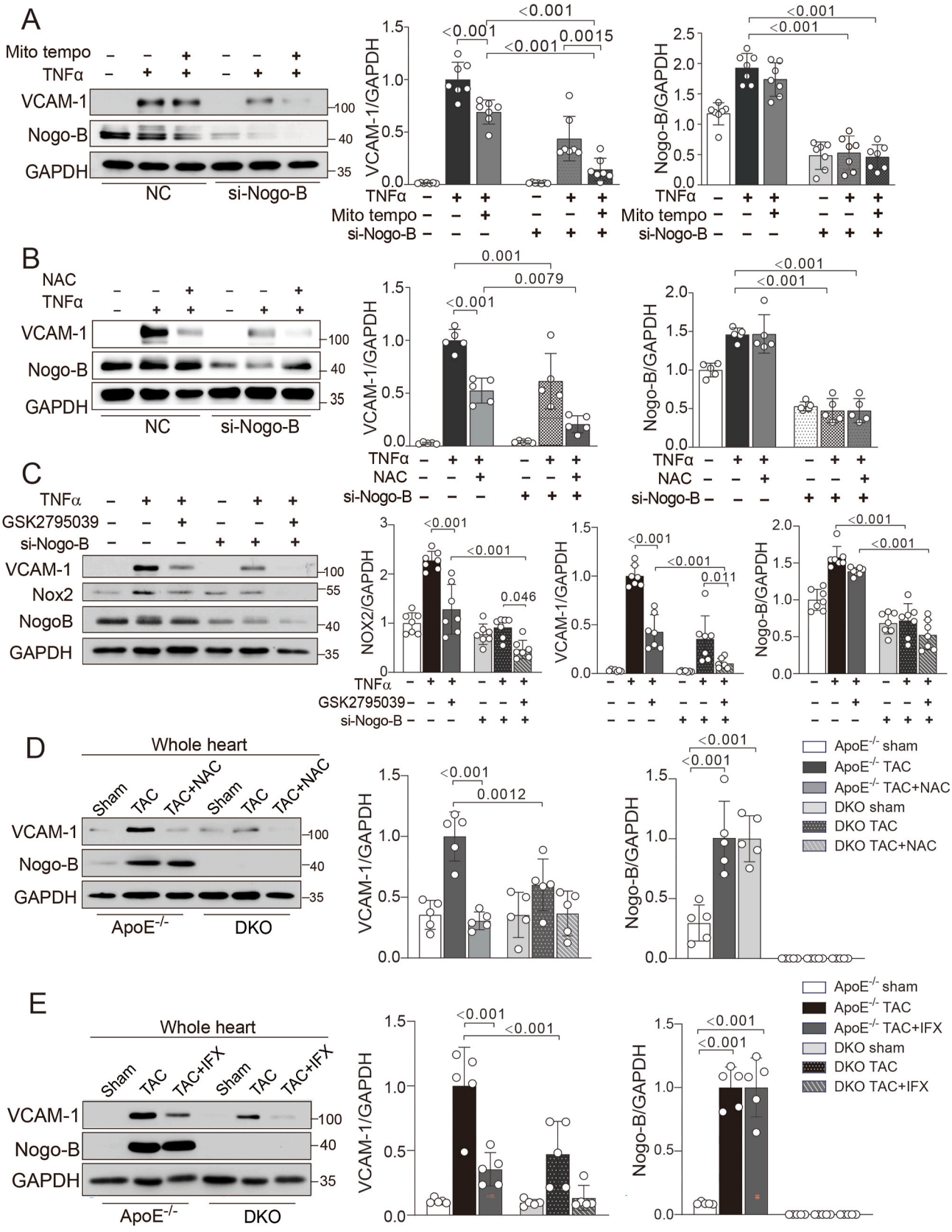

Fig. 6. Nogo-B-activated ROS-p38-p65 pathway was responsible for adhesion molecules upregulation in ECs. (**A-B**) Reprsentative Western blotting images and quantifications of protein levels of VCAM-1 and Nogo-B in HUVECs transfected with NC or si-Nogo-B upon 24-h TNFα stimulation in the presence or absence of 20 μM Mitotempo (**A,** n = 7/group) or 5 mM NAC (**B,** n = 5/group). (**C**) Western blot analysis of VCAM-1, NOX2 and Nogo-B in HUVECs under 24-h TNFα stimuli in the presence or absence of 50 μM GSK2795039 (NOX2 inhibitors). n = 7 per group. (**D-E**) Western blot analysis of VCAM-1 and Nogo-B in whole heart tissue after 24-h TAC treated with vehicle or NAC or infliximab (a chimeric anti-TNFα monoclonal antibody). n = 5/group.

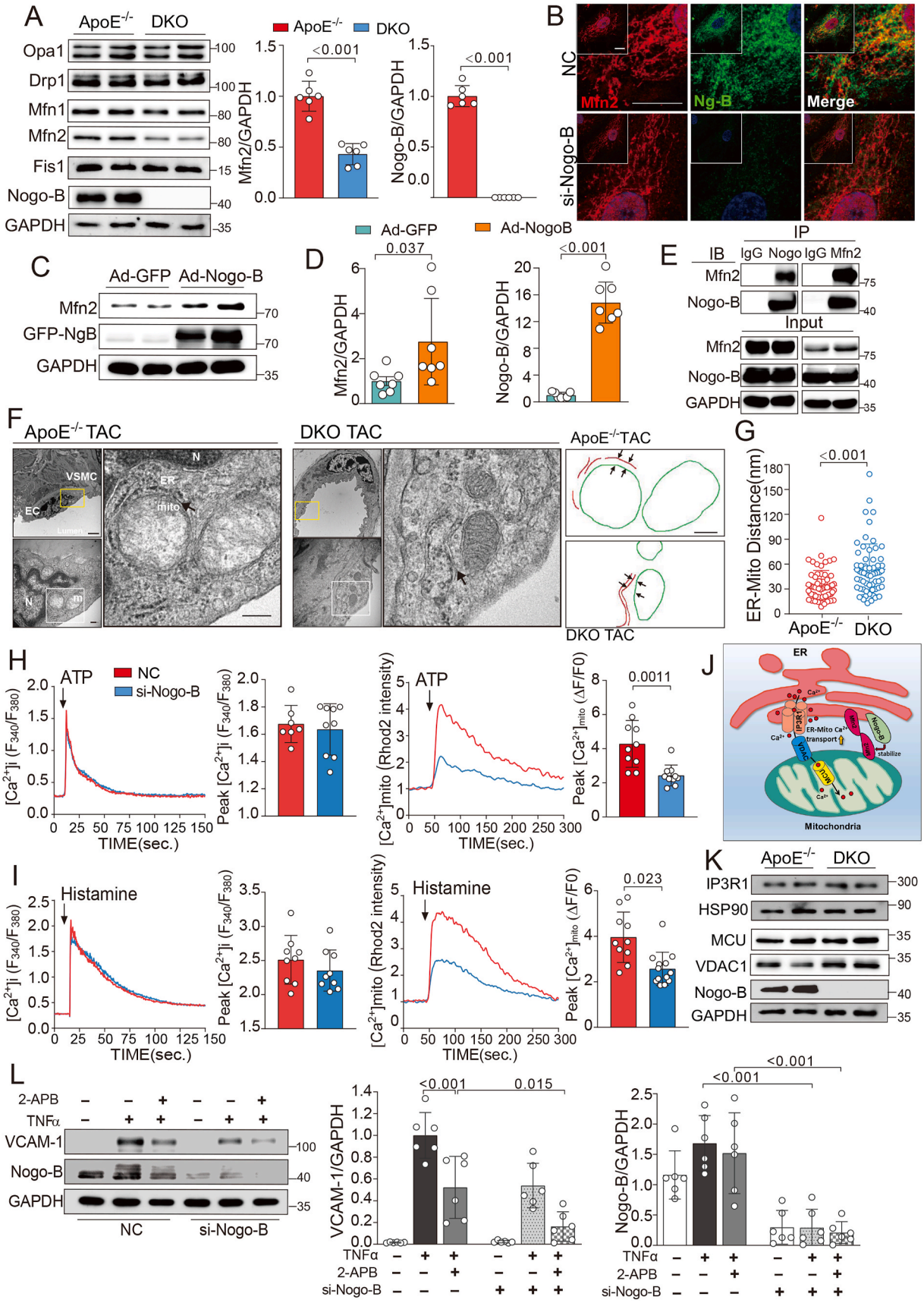

(caption on next page)

Fig. 7. Nogo-B regulated ER-mitochondria tethering and ER-mitochondria Ca^{2+} transport via physical interacting with Mfn2 in endothelial cells. (**A**) Western blot analysis of mitochondrial fission/fusion marker proteins in MCECs isolated from ApoE$^{-/-}$ and DKO hearts of mice. n = 6/group. (**B**) Immunofluorescence staining for Nogo-B (green) and Mfn2 (red) in HUVECs transfected with scrambled (NC) or si-Nogo-B siRNA. Inserts show whole cell images. DAPI stained nuclei. Scale bar: 20 μm. (**C-D**) Western blotting analysis of Mfn2 in HUVECs overexpressed GFP-Nogo-B or GFP. n = 6/group. (**E**) Immunoprecipitation of Nogo-B and blotting with Mfn2 or *vice versa* in HUVECs. (**F**) Representative electron microscopic (EM) images of ER and mitochondria in coronary ECs of 24-h TAC-operated ApoE$^{-/-}$ and DKO mice. Upper left, coronary vessel, Scale bar: 2 μm; lower left, MCECs at higher magnification of the red boxed region, Scale bar: 500 nm; (right panel) mitochondria and ER in MCECs at a higher magnification, Scale bar: 200 nm. The black arrows indicated the ER-mitochondrial distance. (**G**) Statistics of the average ER-mitochondrial distance in 24-h TAC hearts from ApoE$^{-/-}$ and DKO. n ≥ 63 per group. (**H–I**) Representative trace and amplitude statistics of cytosolic and mitochondrial Ca^{2+} transients in HUVECs transfected with NC or Nogo-B siRNA in response to 10 μM ATP or 10 μM histamine stimulation. n ≥ 7 per group for intracellular Ca^{2+} imaging and n≥10 per group for mitochondrial Ca^{2+} imaging. (**J**) Schematic diagram of proteins in MAMs involving in ER-mitochondria Ca^{2+} transport. (**K**) Western blot analysis for selected MAMs proteins in MCECs isolated from ApoE$^{-/-}$ and DKO hearts of mice with TAC. n = 6/group. (**L**) Protein levels of VCAM-1 and Nogo-B in HUVECs under 24-h TNFα stimuli in the presence or absence of 10 μM 2-APB (IP_3Rs inhibitors). n = 7/group. (For interpretation of the references to colour in this figure legend, the reader is referred to the Web version of this article.)

Nogo-B^{ECKO}-ApoE$^{-/-}$ mice compared to age-matched controls (Fig. 8A). Immunofluorescence co-staining of Nogo-B with cell specific marker showed nulled Nogo-B staining in endothelial layer over the coronary plaque (Fig. 8B). Oil Red O staining of sequential heart sections exhibited decreased LCA plaque area at each section along the axis of the aortic root to the apex in TAC-operated Nogo-B^{ECKO}-ApoE$^{-/-}$ mouse hearts compared with ApoE$^{-/-}$ group after 7 weeks (Fig. 8C). Histological analysis of the atherosclerotic plaque in coronary vessels revealed that loss of endothelial Nogo-B significant decreased the severe forms of plaque phenotypes, such as the fibrous cap atheromas and complicated plaque in LCA (Fig. 8D) in addition to reduced atherosclerotic plaque size in the aortic root (Fig. 8E). These results suggest that Nogo-B, acting predominantly in ECs, plays a major role in coronary plaque lesions in ApoE$^{-/-}$ mice with chronic TAC.

4. Discussion

Clinical studies observed elevation of Nogo-B expression in carotid or coronary plaques [17,18], albeit the role of Nogo-B in atherosclerosis remains undefined. In the present study, we revealed that Nogo-B is a

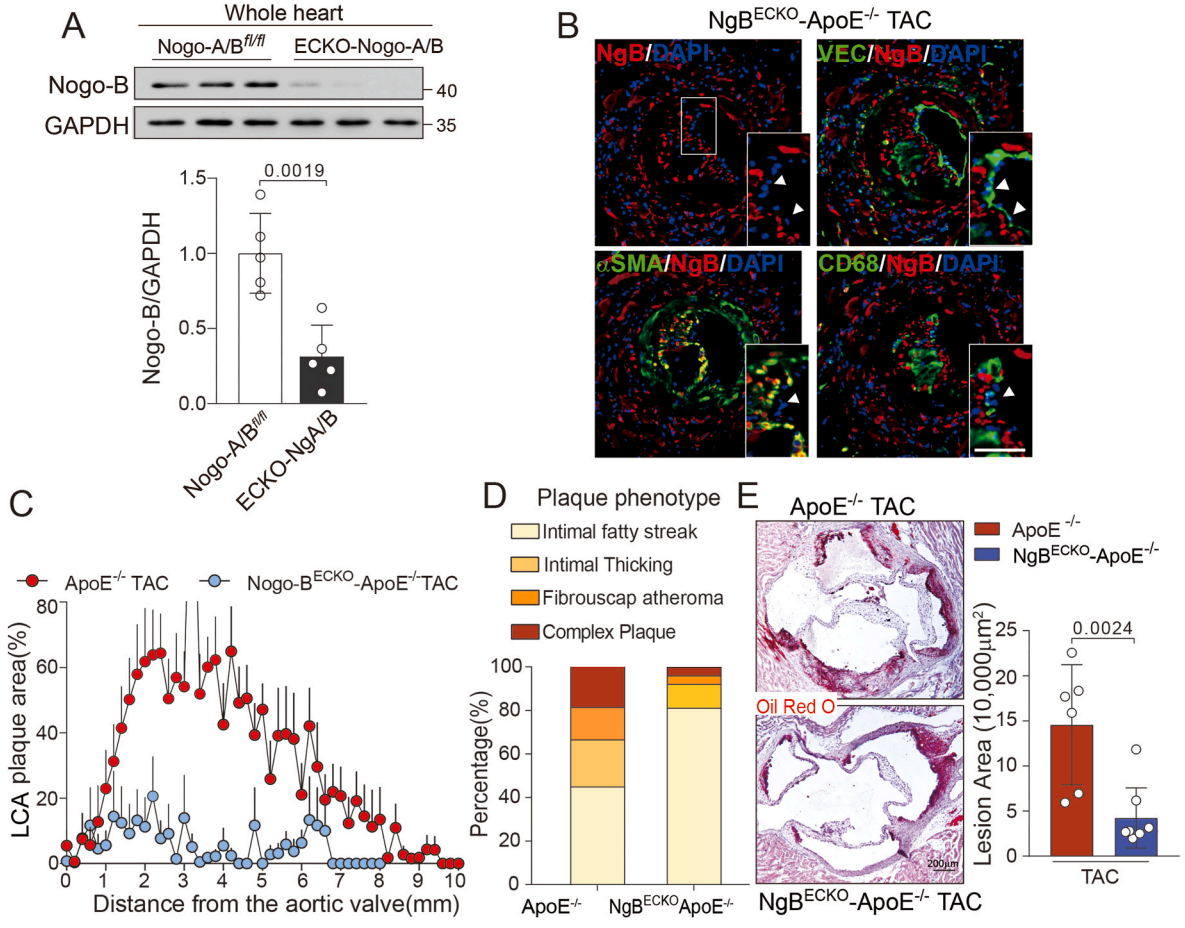

Fig. 8. Lack of endothelial Nogo-B elicited a benign plaque phenotype in ApoE$^{-/-}$ mice. (**A**) Western blot analysis of Nogo-B expression in whole heart tissues from ApoE$^{-/-}$ and Nogo-A/B^{ECKO}-ApoE$^{-/-}$ mice. n = 5 mice/group. (**B**) Immunofluorescence staining of Nogo-A/B (red), with VEC (green), α-SMA (green) and CD68 (green), respectively, in heart sections of Nogo-A/B^{ECKO}-ApoE$^{-/-}$ mice. Scale bar: 50 μm. (**C**) Statistics of LAD plaque area in each section alongside aortic valve to apex in hearts of ApoE$^{-/-}$ and Nogo-A/B^{ECKO}-ApoE$^{-/-}$ mice after 7-week TAC. (n ≥ 6 hearts/group). (**D**) Distribution of LAD plaque phenotypes calculated from each section alongside aortic valve to apex in hearts of ApoE$^{-/-}$ and Nogo-A/B^{ECKO}-ApoE$^{-/-}$ mice subjected to TAC for 7 weeks. Oil Red O stained plaques in serial sections of the whole heart were classified. n ≥ 12 mice/group. (**E**) Representative Oil Red O staining of aortic roots and the quantification of plaque size of ApoE$^{-/-}$ and Nogo-A/B^{ECKO}-ApoE$^{-/-}$ mice after 7-week TAC. n ≥ 6 mice/group. (For interpretation of the references to colour in this figure legend, the reader is referred to the Web version of this article.)

critical promoter of endothelial dysfunction and consequent pathogenesis of coronary atherosclerosis in the settings of hypertension. This conclusion is supported by several sets of *in vivo* and *in vitro* findings. First, Nogo-B upregulation in ECs *in vitro* and *in vivo* by mechano-inflammatory stimuli and deletion of endothelial Nogo-B abolished the upregulation of adhesion molecules and the resultant formation of coronary plaque in ApoE$^{-/-}$ mice. Second, ROS-p38-p65 signaling was involved in Nogo-B mediated upregulation of adhesion molecules in ECs upon inflammatory stimuli. Third, by interacting with Mfn2, Nogo-B regulated ER-mitochondria Ca^{2+} transport thereby controlling mitochondrial ROS generation upon inflammatory stimuli. These findings provide novel insights of Nogo-B in triggering pro-inflammatory phenotype of endothelium and the pathogenesis of coronary atherosclerosis under pressure overload.

Hypertension is a major risk factor of CAD accounting for more than 50% of deaths and disabilities resulting from CAD [40]. Nogo-B is widely expressed in vascular cells and modulates cardiovascular physiology and diseases [41]. We previous reported marked Nogo-B upregulation in the vascular endothelium of wild-type mice subjected to hypertension or pressure overload with exacerbated cardiac hypertrophy or in cultured ECs in response to pro-inflammatory stimuli [20,21]. Here we found that endothelial expression of Nogo-B in ApoE$^{-/-}$ mice significantly elevated in the nascent as well as advanced stages of pressure overload-induced coronary atherosclerosis. We also observed that elevation of Nogo-B in ECs was temporarily associated with upregulation of adhesion molecules (VCAM-1/ICAM-1), which is regarded as the early sign of atherosclerosis. Deletion of Nogo-B in ApoE$^{-/-}$ mice largely prevented upregulation of adhesion molecules and ameliorated atherosclerotic lesions of coronary arteries and aortic roots. These vascular-protective effects by Nogo-B deletion also alleviated cardiac dysfunction and hypertrophy in ApoE$^{-/-}$ mice. To add mechanistic insights into previous clinical findings of elevated expressions of Nogo-B in ECs of human carotid atherosclerotic plaques [17,18], we identified for the first time that Nogo-B is a critical contributor to the initiation of inflammatory phenotypic changes in EC that prelude onset of coronary atherosclerosis and plaque instability.

Cardiac inflammatory cytokines is not constitutively expressed in the physiological heart, but can be induced under stressed conditions such as hypertension [33]. In this study, we confirmed that TNFα together with other inflammatory cytokines (such as IL-1β, IL-6) were significantly elevated in hearts of ApoE$^{-/-}$ mice with TAC. Importantly, blocking TNFα with antibody significantly inhibited TAC-induced VCAM-1 upregulation in ApoE$^{-/-}$ mice. Similarly, we provided evidence for augmented expression of adhesion molecules by OSS in cultured ECs under mechanostress (i.e. OSS). These results verified the close-simulation of cell model to the *in vivo* situation in our study.

Although not acting as the main source of energy supply in ECs, endothelial mitochondria has attracted increasing attention since accumulating studies have indicated its involvement in diverse cardiovascular diseases by modulating the intracellular Ca^{2+}, ROS and nitric oxide signaling [42,43]. Here we revealed heightened mitochondrial oxidative stress in ECs in response to inflammatory stimuli. These alterations in mitochondria paralleled expression levels of Nogo-B, the major isotype of RTN4 in ECs, and associated with facilitated progression of coronary atherosclerosis in ApoE$^{-/-}$ mice with TAC. We determined expression of selected marker proteins that are associated with ER-mitochondrial communication or with mitochondrial morphology. Mfn2 is known to act as a tether fastening the ER with the outer mitochondrial membrane thereby maintaining the intact mitochondria-ER unit, and deficiency of Mfn2 in ECs leads to increased ER-mitochondria distance indicating disruption of ER-mitochondrial connection [38,39]. Nogo-B deficiency did not alter levels of other MAMs-enriched proteins, except for Mfn2. We showed for the first time that physical interaction of Nogo-B with Mfn2 might stabilize Mfn2 as Nogo-B deficiency only selectively reduced protein level of Mfn2 without alteration in mRNA level. Likely as the consequence of attenuated ER-mitochondrial Ca^{2+} transport, we observed in Nogo-B deficient cells reduction in mitochondrial Ca^{2+} level without change in the cytosolic Ca^{2+} kinetics. These findings point to Mfn2 as the critical molecular target of Nogo-B in regulating ER-mitochondria communications, mitochondrial function and oxidative stress.

Being a hallmark of the preclinical stage of atherosclerosis, endothelial dysfunction plays a pivotal role in the development of atherosclerotic disease, but the signaling pathway remains incomplete identified [5,6]. Here we found that Nogo-B was upregulated in the endothelium of coronary arteries of ApoE$^{-/-}$ mice from 24 h post-TAC and afterwards. In cultured ECs, we simulated *in vivo* pressure-overload conditions by applying OSS or inflammatory cytokines, stimuli that quickly activated ROS generation and p38-p65 phosphorylation. Importantly, these changes were abolished by siRNA Nogo-B knockdown or blocking ROS with NAC, suggesting that in ApoE$^{-/-}$ mice with TAC, Nogo-B acts as a trigger to enhance oxidative stress and p38-p65 signaling in ECs. Complementing to the established ROS-p38-p65 signaling axis [44,45], our findings identified Nogo-B as a novel component in this pro-inflammatory pathway leading to EC dysfunction and coronary atherosclerosis.

Notably, Nogo-B is highly expressed in multiple cell types but its function is distinct depending on cell types. For example, there was a negative correlation between ER-mitochondria connection and Nogo-B expression level in HeLa cells [12], but both indices were positively correlated in VSMCs [13,14], as well as in ECs as shown in the present study. Both systemic and EC-specific Nogo-B deletion similarly attenuated the coronary atherosclerosis evoked by TAC, indicating the pivotal role of endothelial Nogo-B in our *in vivo* model that combined both abnormal lipid metabolism and hypertension. Our genetic manipulation of Nogo-A/B gene would also deplete Nogo-A, which is not expressed in ECs [16], but in non-EC cell types like VSMCs or macrophages, that are rich in arterial atherosclerotic plaques. Thus, we cannot exclude the additional contribution of Nogo-A depletion to the findings in the present study.

Taken together, the present study documented in pressure-overloaded ApoE$^{-/-}$ mouse hearts that coronary endothelial Nogo-B is a novel contributor to atherogenic endothelial dysfunction by augmenting mitochondrial oxidative stress and the downstream p38-p65 signaling with enhanced inflammation. The convergence of several pathological processes evoked by upregulation of the endothelial Nogo-B signaling makes it a potential common therapeutic target in settings of hypertension and atherosclerosis.

Sources of funding

This work was supported by grants from National Nature Science Foundation of China (31871153, 32171103, 31971045, 82170298, 82070393); China Postdoctoral Science Foundation (2018M631174 and 2019T120919); Postdoctoral Research Program of Shaanxi (2018BSHYDZZ73); and Natural Science Basic Research Program of Shaanxi (2022JM-557).

Declaration of competing interest

The authors declare that there are no confilct of interests.

Data availability

Data will be made available on request.

Acknowledgements

We are grateful to Ying Hao (Instrumental Analysis Center of Xi'an Jiaotong University), Xiao-Fei Wang and Lin Han (Biomedical Experimental Center of Xi'an Jiaotong University) for their technical support.

Appendix A. Supplementary data

Supplementary data to this article can be found online at https://doi.org/10.1016/j.redox.2023.102944.

References

[1] A.K. Malakar, et al., A review on coronary artery disease, its risk factors, and therapeutics, J. Cell. Physiol. 234 (10) (2019) 16812–16823.
[2] P.G. Steg, G. Ducrocq, Future of the prevention and treatment of coronary artery disease, Circ. J. 80 (5) (2016) 1067–1072.
[3] Y. Matsuzawa, A. Lerman, Endothelial dysfunction and coronary artery disease: assessment, prognosis, and treatment, Coron. Artery Dis. 25 (8) (2014) 713–724.
[4] D.J. Medina-Leyte, et al., Endothelial dysfunction, inflammation and coronary artery disease: potential biomarkers and promising therapeutical approaches, Int. J. Mol. Sci. 22 (8) (2021) 3850.
[5] M.A. Gimbrone, G. Garcia-Cardena, Endothelial cell dysfunction and the pathobiology of atherosclerosis, Circ. Res. 118 (4) (2016) 620–636.
[6] C. Souilhol, et al., Endothelial responses to shear stress in atherosclerosis: a novel role for developmental genes, Nat. Rev. Cardiol. 17 (1) (2020) 52–63.
[7] S. Godo, H. Shimokawa, Endothelial functions, Arterioscler. Thromb. Vasc. Biol. 37 (9) (2017) e108–e114.
[8] I. Tabas, G. Garcia-Cardena, G.K. Owens, Recent insights into the cellular biology of atherosclerosis, J. Cell Biol. 209 (1) (2015) 13–22.
[9] U. Forstermann, N. Xia, H. Li, Roles of vascular oxidative stress and nitric oxide in the pathogenesis of atherosclerosis, Circ. Res. 120 (4) (2017) 713–735.
[10] M. Batty, M.R. Bennett, E. Yu, The role of oxidative stress in atherosclerosis, Cells 11 (23) (2022) 3843.
[11] G.K. Voeltz, et al., A class of membrane proteins shaping the tubular endoplasmic reticulum, Cell 124 (3) (2006) 573–586.
[12] R.J. Carter, et al., Novel roles of RTN4 and CLIMP-63 in regulating mitochondrial structure, bioenergetics and apoptosis, Cell Death Dis. 13 (5) (2022) 436.
[13] Y.D. Yang, et al., Nogo-B receptor directs mitochondria-associated membranes to regulate vascular smooth muscle cell proliferation, Int. J. Mol. Sci. 20 (9) (2019) 2319.
[14] G. Sutendra, et al., The role of Nogo and the mitochondria-endoplasmic reticulum unit in pulmonary hypertension, Sci. Transl. Med. 3 (88) (2011) 88ra55.
[15] J.P. Sarkey, et al., Nogo-A knockdown inhibits hypoxia/reoxygenation-induced activation of mitochondrial-dependent apoptosis in cardiomyocytes, J. Mol. Cell. Cardiol. 50 (6) (2011) 1044–1055.
[16] L. Acevedo, et al., A new role for Nogo as a regulator of vascular remodeling, Nat. Med. 10 (4) (2004) 382–388.
[17] K. Drozdz, et al., Nogo-B expression, in arterial intima, is impeded in the early stages of atherosclerosis in humans, APMIS 122 (9) (2014) 742–749.
[18] J.A. Rodriguez-Feo, et al., Low levels of Nogo-B in human carotid atherosclerotic plaques are associated with an atheromatous phenotype, restenosis, and stenosis severity, Arterioscler. Thromb. Vasc. Biol. 27 (6) (2007) 1354–1360.
[19] A. Di Lorenzo, et al., Endothelial reticulon-4B (Nogo-B) regulates ICAM-1-mediated leukocyte transmigration and acute inflammation, Blood 117 (7) (2011) 2284–2295.
[20] Y. Zhang, et al., Endothelial Nogo-B regulates sphingolipid biosynthesis to promote pathological cardiac hypertrophy during chronic pressure overload, JCI Insight 1 (5) (2016), e85484.
[21] A. Cantalupo, et al., Nogo-B regulates endothelial sphingolipid homeostasis to control vascular function and blood pressure, Nat. Med. 21 (9) (2015) 1028–1037.
[22] J.J. Li, et al., Endothelial K(Ca)3.1 and K(Ca)2.3 mediate S1P (Sphingosine-1-Phosphate)-Dependent vasodilation and blood pressure homeostasis, Arterioscler. Thromb. Vasc. Biol. 43 (5) (2023) 726–738.
[23] J.M. Meves, et al., Oligodendrocytic but not neuronal Nogo restricts corticospinal axon sprouting after CNS injury, Exp. Neurol. 309 (2018) 32–43.
[24] M.X. Quan, et al., MST1 suppresses disturbed flow induced atherosclerosis, Circ. Res. 131 (9) (2022) 748–764.
[25] Y. Zhang, et al., Stretch-induced sarcoplasmic reticulum calcium leak is causatively associated with atrial fibrillation in pressure-overloaded hearts, Cardiovasc. Res. 117 (4) (2021) 1091–1102.
[26] J. Baardman, et al., Macrophage ATP citrate lyase deficiency stabilizes atherosclerotic plaques, Nat. Commun. 11 (1) (2020) 6296.
[27] Y. Qi, et al., Excess sarcoplasmic reticulum-mitochondria calcium transport induced by Sphingosine-1-phosphate contributes to cardiomyocyte hypertrophy, Biochim. Biophys. Acta Mol. Cell Res. 1868 (5) (2021), 118970.
[28] Z.H. Zhang, et al., PPARδ agonist prevents endothelial dysfunction via induction of dihydrofolate reductase gene and activation of tetrahydrobiopterin salvage pathway, Br. J. Pharmacol. 176 (16) (2019) 2945–2961.
[29] W. Wu, et al., Activation of Hippo signaling pathway mediates mitochondria dysfunction and dilated cardiomyopathy in mice, Theranostics 11 (18) (2021) 8993–9008.
[30] A. Marino, et al., Pressure overload leads to coronary plaque formation, progression, and myocardial events in ApoE$^{-/-}$ mice, JCI Insight 4 (9) (2019), e128220.
[31] C. Silvestre-Roig, et al., Atherosclerotic plaque destabilization: mechanisms, models, and therapeutic strategies, Circ. Res. 114 (1) (2014) 214–226.
[32] Y. Nakashima, et al., Upregulation of VCAM-1 and ICAM-1 at atherosclerosis-prone sites on the endothelium in the ApoE-deficient mouse, Arterioscler. Thromb. Vasc. Biol. 18 (5) (1998) 842–851.
[33] M. Sun, et al., Tumor necrosis factor-alpha mediates cardiac remodeling and ventricular dysfunction after pressure overload state, Circulation 115 (11) (2007) 1398–1407.
[34] M.G. von Brandenstein, et al., A p38-p65 transcription complex induced by endothelin-1 mediates signal transduction in cancer cells, Biochim. Biophys. Acta 1783 (9) (2008) 1613–1622.
[35] I. Dolado, et al., p38alpha MAP kinase as a sensor of reactive oxygen species in tumorigenesis, Cancer Cell 11 (2) (2007) 191–205.
[36] B. Canovas, A.R. Nebreda, Diversity and versatility of p38 kinase signalling in health and disease, Nat. Rev. Mol. Cell Biol. 22 (5) (2021) 346–366.
[37] D.B. Zorov, M. Juhaszova, S.J. Sollott, Mitochondrial reactive oxygen species (ROS) and ROS-induced ROS release, Physiol. Rev. 94 (3) (2014) 909–950.
[38] O.M. de Brito, L. Scorrano, Mitofusin 2 tethers endoplasmic reticulum to mitochondria, Nature 456 (7222) (2008) 605–610.
[39] R. Filadi, E. Greotti, P. Pizzo, Highlighting the endoplasmic reticulum-mitochondria connection: focus on Mitofusin 2, Pharmacol. Res. 128 (2018) 42–51.
[40] S.S. Lim, et al., A comparative risk assessment of burden of disease and injury attributable to 67 risk factors and risk factor clusters in 21 regions, 1990-2010: a systematic analysis for the Global Burden of Disease Study 2010, Lancet 380 (9859) (2012) 2224–2260.
[41] L. Sasset, et al., Sphingolipid de novo biosynthesis: a rheostat of cardiovascular homeostasis, Trends Endocrinol. Metabol. 27 (11) (2016) 807–819.
[42] S.M. Davidson, M.R. Duchen, Endothelial mitochondria: contributing to vascular function and disease, Circ. Res. 100 (8) (2007) 1128–1141.
[43] S.M. Davidson, Endothelial mitochondria and heart disease, Cardiovasc. Res. 88 (1) (2010) 58–66.
[44] A. Reustle, M. Torzewski, Role of p38 MAPK in atherosclerosis and aortic valve sclerosis, Int. J. Mol. Sci. 19 (12) (2018) 3761.
[45] I. Corre, F. Paris, J. Huot, The p38 pathway, a major pleiotropic cascade that transduces stress and metastatic signals in endothelial cells, Oncotarget 8 (33) (2017) 55684–55714.